Original Research Article

Development of WC-Inconel composites using selective laser melting

Check for updates

Q.B. Nguyen [a,*], Z. Zhu [a], B.W. Chua [a], W. Zhou [b], J. Wei [a,*], S.M.L. Nai [a,*]

[a] Singapore Institute of Manufacturing Technology, 73 Nanyang Dr, Singapore 637662, Singapore
[b] School of Mechanical & Aerospace Engineering College of Engineering, Nanyang Technological University, 50 Nanyang Ave, 639798, Singapore

ARTICLE INFO

ABSTRACT

In the present study, selective laser melting (SLM) was used to successfully fabricate Inconel 718–tungsten carbide (WC) composites. The processing parameter optimization results reveal that nearly non-porous composites (99.54%) were achieved with the laser power of 220 W, scanning speed of 850 mm s^{-1}, and the hatch spacing of 150 μm. The microstructural characterization unveils that elongated grain structure in the heat flow direction was observed in the case of pure IN718 while WC particles served as obstacles to hinder the grain growth in the composites. The formation of in situ intermediate layer and the strong interfacial bonding between WC super-hard particles and the matrix acted as load bearing and significantly contribute to the overall properties of composites. Mechanical tests indicate significant improvements of microhardness and tensile strengths, although a drop in strength was observed when the amount of WC reached 15 wt.%. In addition, the thermal experiment shows that the composites are dimensionally stable at higher temperature compared to their monolithic counterpart. The findings suggest that the developed IN718-WC composites can be utilized in many critical engineering applications in nuclear sector.

1. Introduction

Inconel 718 (IN718) is one of the most commonly used nickel super-alloys which are mainly employed in high temperature and erosive environmental applications such as in aerospace's engines [1], turbines [2], and nuclear reactors [3] due to its high mechanical properties and excellent corrosive resistance. The main drawbacks of Inconel alloys are their low hardness and wear resistance as well as the machining difficulty [4].

In recent years, scientists and researchers around the globe have been attracted by a revolutionized additive manufacturing technology, particularly selective laser melting (SLM) [5], which is able to handle complicated structural features effectively at a much shorter time and affordable price [6]. In this SLM process, the 3D CAD drawing object is sliced into hundreds to thousands of very thin layers depending on the object height of typically 20–60 μm thickness for each layer [7]. The machine would next read each layer and coat powder with the same layer thickness. Subsequently, the laser selectively

melts the powder according to the CAD drawing in that layer. The process is continuously repeated till the object is completely built and the excess powder is recycled [8].

The literature shows that some attempts have been done to integrate carbide, boride and oxide reinforcements into the metal matrix or apply hard coatings on the surface to improve working condition of the composites [9,10]. Cooper et al. attempted to reinforce micron-TiC, SiC and Al_2O_3 particles into Inconel 625 matrix using the laser powder bed fusion process successfully, however, cracks, high porosity level and distortion were reported as the key challenges [11]. In another instance, Rong et al. used various laser energy intensities to add 25 wt.% of WC_{1-x} to Inconel 718 and were only able to achieve a maximum density of 98.3% [12].

Moreover, many efforts have been carried out using variable processing parameters in accordance with machine manufacturers' guidelines to achieve high density Inconel printed parts (>99%) [13,14]. The processing inputs, namely energy intensity (laser power versus scanning speed), hatch spacing and powder characteristics, in particular, shape, size, morphology and layer thickness are the key contributors to the quality of 3D built parts [15].

Accordingly, in the present study, an attempt is made to integrate tungsten carbide (WC) particles into Inconel 718 matrix to form IN718-WC composites using a SLM Concept Laser M2 at higher laser power (e.g. >200 W) to improve not only microhardness and wear resistance but also tensile strength and microstructure. A laser power optimization study is also carried out to achieve the maximum printed parts' density (>99% dense). Moreover, the relationship between microstructure and mechanical properties are discussed.

2. Experimental procedure

2.1. Materials

Monolithic Inconel 718 (IN718) spherical powder with an average powder size of 31 μm was provided by Concept Laser with the chemical composition and morphology as shown in Table 1 and Fig. 1, respectively. In addition, the plasma spheroidized WC powder with a particle size distribution from 15 to 53 μm was purchased from Tekna Canada (Fig. 1). Characteristics such as particle size distribution, density and

Table 1 – Chemical composition of Inconel 718 powder (wt.%).

Sample	Ni	Ti	Cr	Mo	Nb	Fe	C	Mn	Si	Al	Co	Cu
IN718	53.07	0.96	19.33	2.99	5.2	Bal	0.028	0.07	0.06	0.5	0.29	0.048
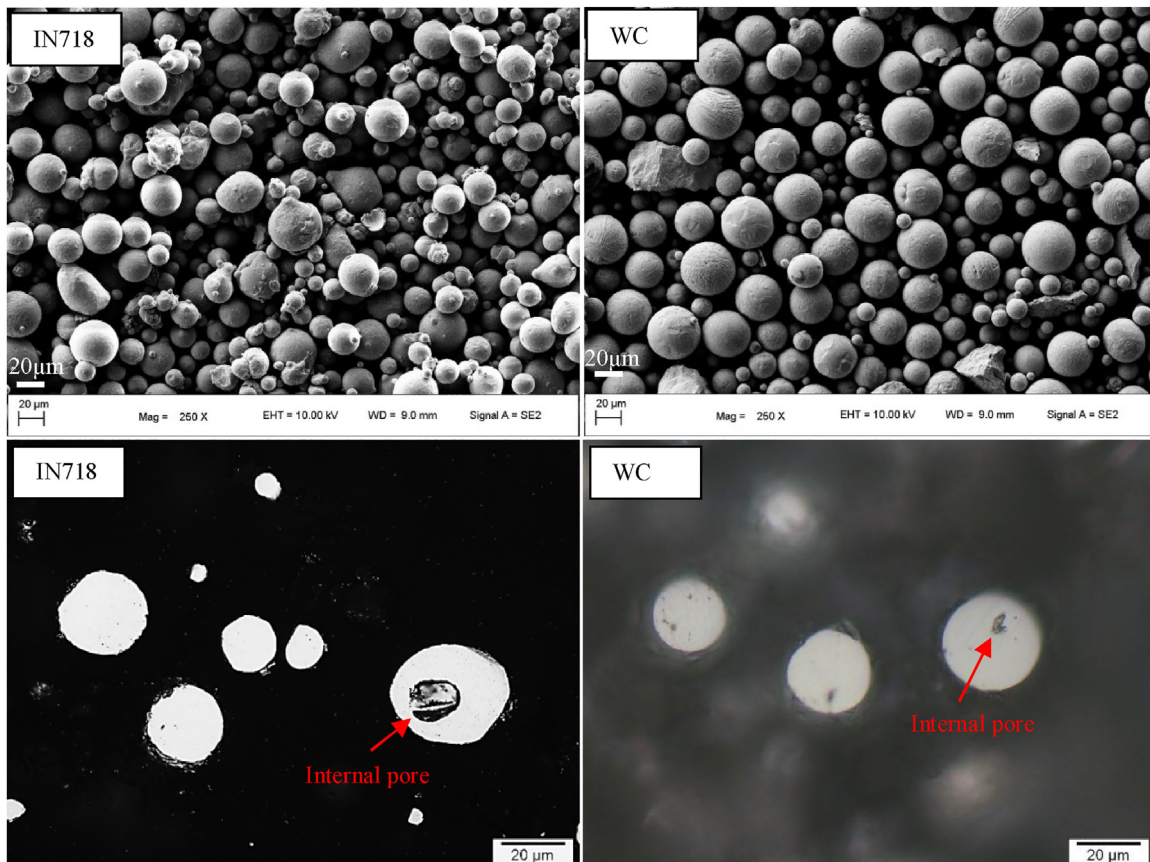
Fig. 1 – Particle morphology of IN718 powder and WC powder (the scale bar: 20 μm).

Table 2 – Particle size distribution and densities of IN718 and WC powders.

Material	Particle size (μm)			Density (g/cm^3)		
	D10	D50	D90	Apparent	Tapped	True
IN718	21.37 ± 0.43	31.24 ± 0.97	49.52 ± 0.76	3.8780 ± 0.0172 (47.4% dense)	4.9123 ± 0.0153 (60% dense)	8.1794 ± 0.0059
WC	22.59 ± 0.62	32.71 ± 1.05	51.36 ± 1.21	9.5205 ± 0.0211 (56% dense)	10.2047 ± 0.0252 (60% dense)	17.0521 ± 0.0185

Table 3 – Flow characteristics of IN718 and WC powders.

Material	BFE (mJ)	SI	FRI	SE (mJ/g)	Flow rate (s/50 g)
IN718	1070 ± 5	1.03 ± 0.04	1.18 ± 0.02	3.96 ± 0.07	28.35 ± 0.32
WC	1201 ± 9	1.05 ± 0.06	1.19 ± 0.05	1.94 ± 0.06	5.43 ± 0.26

BFE: basic flow energy; SI: stability index; FRI: flow rate index; SE: specific energy.

flowability of IN718 and WC powders are presented in Tables 2 and 3 [16]. Three weight percentages of WC powder (5, 10, and 15 wt.%) were blended with IN718 powder for 5 h using a universal Inversina mixer to achieve homogeneous mixture prior to the printing process.

2.2. SLM methodology

In the present study, a newly acquainted Concept Laser M2 equipped with a dual 400 W Ytterbium laser system was used to fabricate the IN718 and its composite samples in the forms of $10 \times 10 \times 10$ mm cubes and tensile bars according to ASTM-E8 as shown in Fig. 2. The standard processing parameters (laser power of 180 W, scanning speed of 850 mm s^{-1}, laser spot of 130 μm, hatch spacing of 150 μm, and powder layer thickness of 25 μm) for island scanning strategy were firstly used to produce 99.87% dense monolithic IN718 sample. Subsequently, four different laser powers (180 W, 200 W, 220 W and 240 W) were employed to determine the optimal condition in terms of minimal porosity and microstructural integrity for processing the IN718-5WC composite before applying the same processing parameters for the other composites (IN718-10WC and IN718-15WC).

2.3. Density measurement

Density of powders was characterized using different density measurement methods. Apparent, tapped and true density were measured in accordance with ASTM B212, B527, and B923 using the Hall flow meter and pycnometer methods, respectively. In addition, the bulk density of printed samples was determined using the Archimedes' principle (Table 2, Figs. 3 and 4).

2.4. X-ray diffraction study

The presence of dominant phases in the powder and printed samples was examined using an automated X-ray diffractometer (Bruker, D8 Discovery) with Cu$_\alpha$ radiation (wavelength of 1.54056 Å) and a scanning speed of 2 degree/min (Fig. 5).

2.5. Microstructure characterization

Microstructural characterization studies using optical microscopy (OM) and scanning electron microscopy (JEOL JSM-
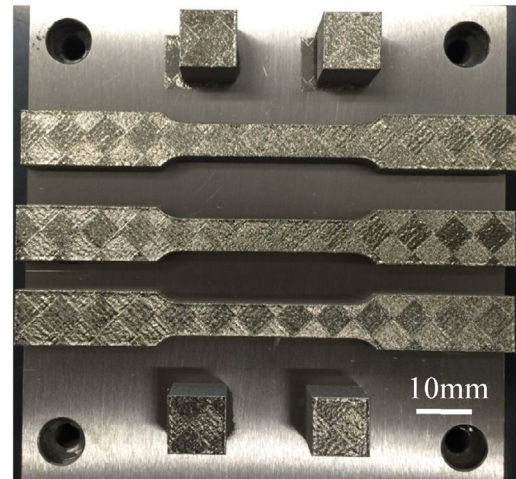
Fig. 2 – Photo showing the printed cubes and tensile coupons.

IT300LV) equipped with EDX were conducted on metallographically polished IN718 and its composite samples to show the level of porosity as well as the distribution of WC particle and the interface between particle and the matrix. Waterless Kalling's reagent (5 g CuCl$_2$, 100 ml HCl, 100 ml ethanol) was used to reveal the scanning pattern, grain structure, and in situ intermediate layer at the particle–matrix interface. In addition, the fracture surface of tensile samples was characterized using OM and SEM in order to provide insights into the fracture mechanisms operating under tensile loading.

2.6. Thermal mechanical study

The thermal behavior of monolithic IN718 and composite samples was conducted using a thermal mechanical analysis Q400 equipment in the temperature range from 50 to 700 °C with a ramping rate of 5 °C min^{-1}. The coefficient of thermal expansion (CTE) was derived from the experiment to study the dimensional stability of the monolithic and composite samples.
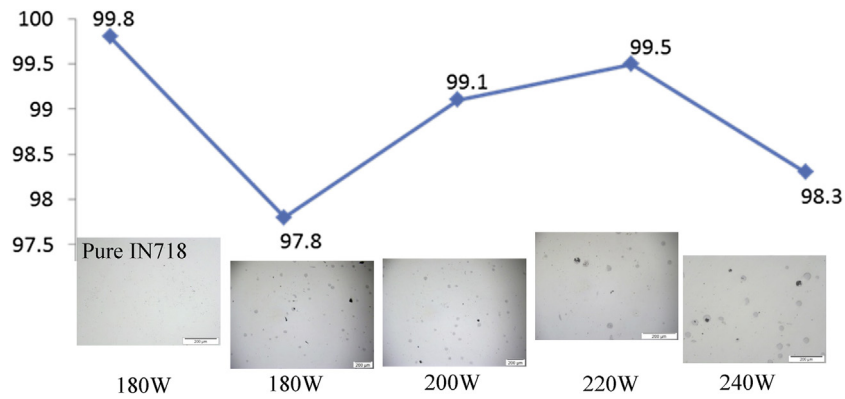
Fig. 3 – Density variation with respect to laser power for IN718-5WC composite samples (the scale bar: 200 μm).
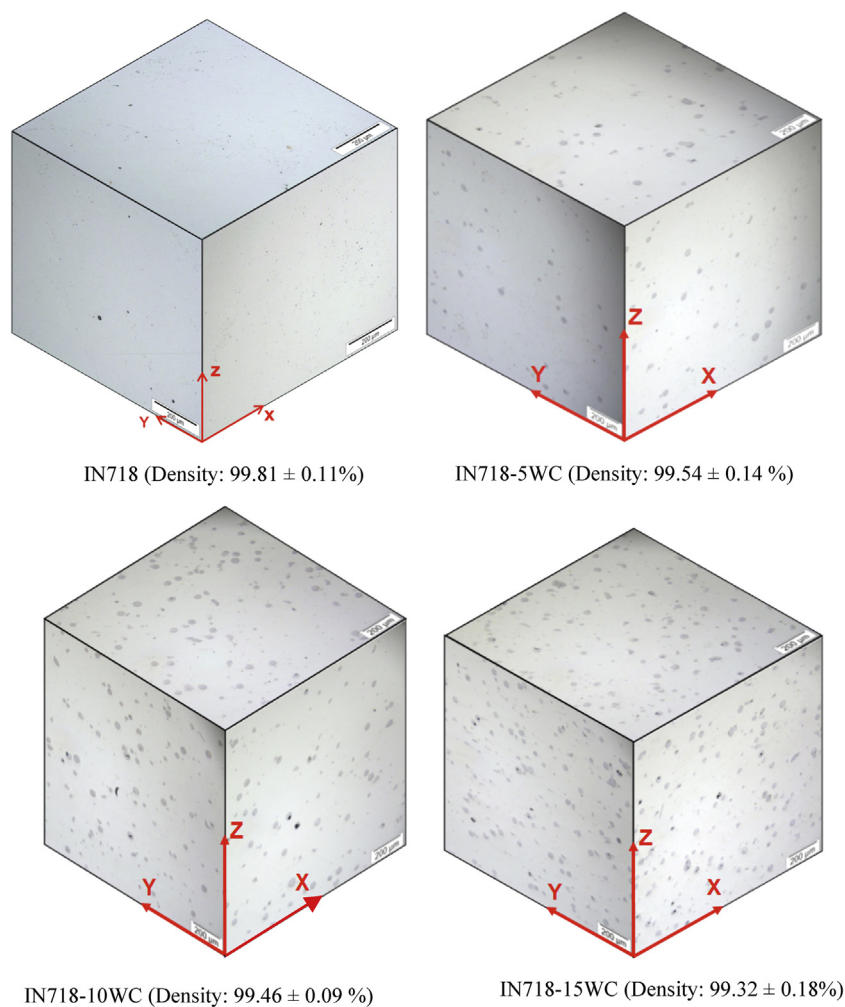

Fig. 4 – OM images of monolithic IN718 and its composites (the scale bar: 200 μm).

2.7.   Microhardness and tensile test

Microhardness measurements were made on the polished samples. Vicker microhardness was measured using an automated digital microhardness tester using an indenting load of 200 gf and a dwell time of 15 s. Furthermore, Brinell hardness was used to measure the overall hardness of the monolithic and composite sample matrices.

A universal Instron-5982 testing system was used to carry out the tensile test on the as-printed tensile bar in accordance with ASTM E8M-05 with a strain rate of $10^{-4}\,\text{s}^{-1}$. An advanced video extensometer using a high resolution camera was employed to record the strain of tensile samples.
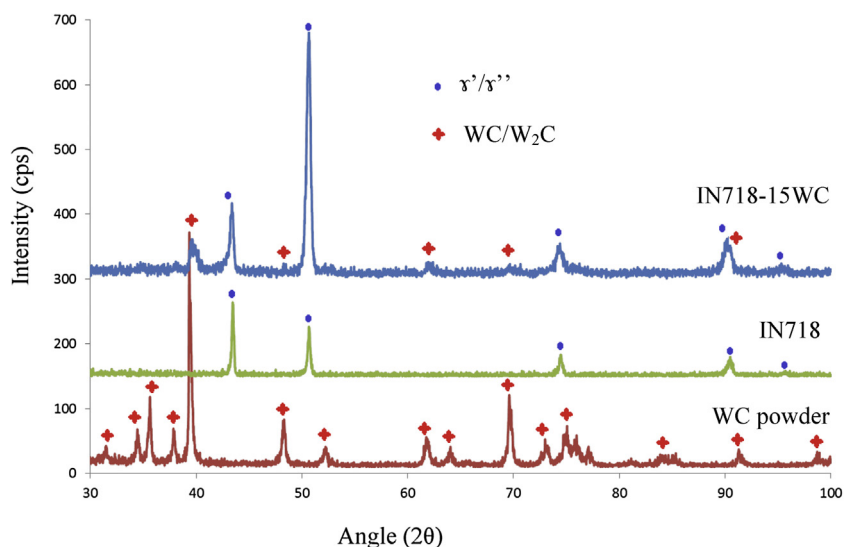
Fig. 5 – X-ray diffraction results of IN718 and IN718-15WC printed samples.

3. Results and discussion

3.1. Powder characteristics

Characteristics of IN718 and WC powders were determined using different characterization tools to assess their suitability for additive manufacturing. Both powders are generally in the spherical morphology (Fig. 1) which promotes the flowability and uniform powder spreading during the powder raking process [17]. The characteristics of IN718 and WC powders in Tables 2 and 3 reveal that the particle size distribution of two powders was similar and ideal to be used in the SLM process in which the bigger powder size is generally less than 63 μm [14]. The maximum packing density (tapped density over true density) of both powders was found to be 60%. In addition, the rheological flowability results in Table 3 indicate that both powders flow stably with the same required energy from cycle 1 to cycle 7, and the WC powder required higher energy to flow although it flows much faster when compared to that of IN718 powder. This is attributed to its smoother surface and higher specific density. Furthermore, the presence of irregular shaped particles and satellites in the IN718 samples affected its flowability (Fig. 1).

However, these powders were found to have internal porosity due to the entrapment of gas during the gas and plasma spheroidized atomization process and this may have adverse effects on the properties of the printed parts in the case the powders were not melted completely and trapped gas was not released. The particle size distribution results reveal that both powders have similar size ranging from 15 to 53 μm. This was to ensure that both powders are well mixed together using the Inversina mixer and to avoid the segregation phenomenon owing to density differences [18].

3.2. Optimization of processing parameters

The monolithic Inconel 718 samples were fabricated using the standard parameter setting provided by the Concept Laser manufacturer. However, due to significant difference in the melting point between IN718 (1336 °C) and WC (2870 °C) powders, further parameter optimization was necessary to achieve maximum density of the composites [19]. Subsequently, four different laser powers (180 W, 200 W, 220 W and 240 W) were selected and 3 cubes of $10 \times 10 \times 10$ mm were printed for density measurement for each laser setting, for IN718-5WC composite samples. The density measurement results reveal that the density of composite sample increased with the increasing laser power and peaked at 220 W (99.54% dense) (Fig. 3). However, with further increase in laser power, significant black soot and the formation of spatter due to high thermal gradient was visually observed. This was the reason led to detrimental effect on the densification of the composite samples. The optimized laser power (220 W) was subsequently applied to print cubes and tensile bars as seen in Fig. 2 for all the composites, IN718-5WC, IN718-10WC and IN718-15WC samples which resulted in high density of 99.54%, 99.46% and 99.32%, respectively (Fig. 4). In addition, density measurement and defect detection using X-ray CT is recommended for better measurement accuracy [20].

3.3. Microstructural characterization

The X-ray diffraction study detected the presence of both γ' $(Al_{0.5}Ti_{0.5})Ni_3$ and γ'' (Ni_3Nb) phases in the IN718 powder as well as in the IN718 printed samples (Fig. 5). These two phases were reported to be present in the nano-scale spheroidal and elongated disc forms and assisted in matrix strengthening mechanism [15,19,21]. Similarly, the tungsten carbide powder contains not only WC phase but also W_2C phase. All these phases were detected in the final composite samples as shown in Fig. 5. It is noted that the strongest peak of monolithic IN718 samples was at (111) plane (43.5°) while that of composite samples was shifted to (200) plane (50.6°). This texture change would affect the slip mechanism and finally the microstructure and mechanical properties of the composites [15].

The samples were grinded and polished in the X, Y, and Z directions to reveal any micro-pore and defects under optical microscopy as shown in Fig. 4. It is observed that minimal porosity and/or trace of spatter formation were seen in the monolithic and composite samples. Those pores are typically round with a diameter of less than a few μm and this is because some of the gas between powders were trapped during a micro-second heating and solidification process [6]. In addition, the inherent pore inside the WC particles was seen in all composite samples and their presence increased with the increasing amount of WC reinforcement. Despite the observed porosity, the results of density measurement for all monolithic and composite samples shown in Fig. 4 also reveal that very dense composites were successfully fabricated with the optimized processing parameters [19].

An attempt was carried out to reveal the scanning pattern and the grain structure of monolithic and composite samples by etching the polished samples with Kalling's reagent using immersion method (Figs. 6 and 7). The scanning pattern in the X and Y directions looked like fish-scale shape with the width of 130–150 μm and depth of 100–150 μm while an island scanning pattern with the width between two scanned lines of 60–70 μm was observed in the Z direction for all monolithic

and composite samples. In addition, grain feature was presented in Fig. 7 for the monolithic IN718 and IN718-15WC samples in X direction. It is obviously seen that elongated grain structure was present in the monolithic sample in the heat flow direction from the top to bottom and the grains varied significantly from place to place [22]. However, with the addition of WC particles, the grain structure became much finer with less elongated grain in the heat flow direction. The high energy laser triggered and melted the IN718 matrix, the generated heat was then conducted to the lower layers and encountered WC particles where they acted as a heat seal, the grain growth was thus obstructed by these unmelted particles.

A deeper and closer look at the microstructure of the composites using scanning electron microscopy to examine the distribution of WC particles and the interface between the particle and the matrix (Fig. 8). WC particles were observed to be well distributed in the IN718 matrix with good interfacial bonding and no void or pore was observed at the interface. A high magnification image (Fig. 9) shows the formation of an in situ intermediate layer [12,18]. With the support of EDX function, the significant presence of Cr and Fe at the interface was revealed. It is presumed that a chemical reaction took
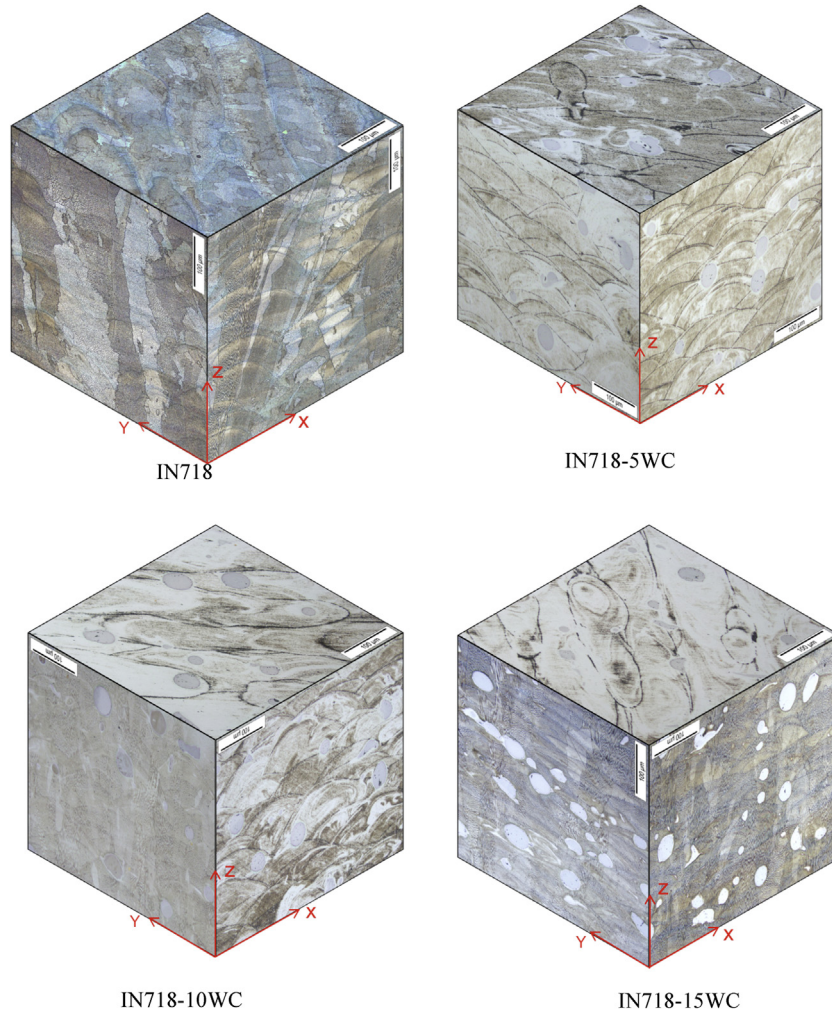

Fig. 6 – OM images showing the scanning pattern and grain structure of monolithic IN718 and composites (the scale bar: 100 μm).

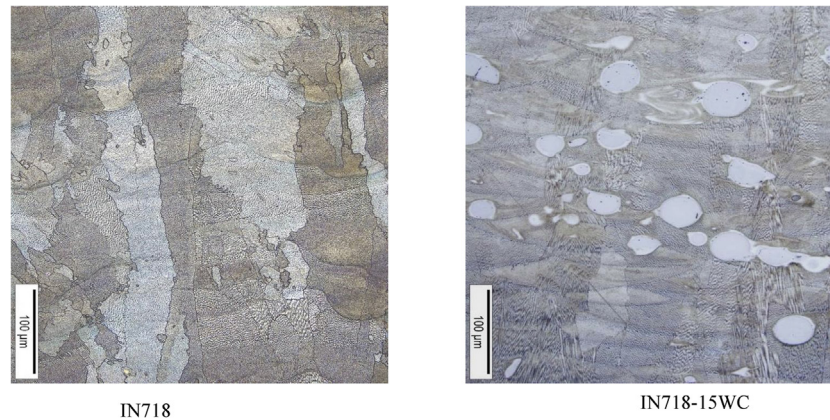IN718   IN718-15WC

Fig. 7 – Representative OM images showing the effect of WC particles in controlling the grain structure.
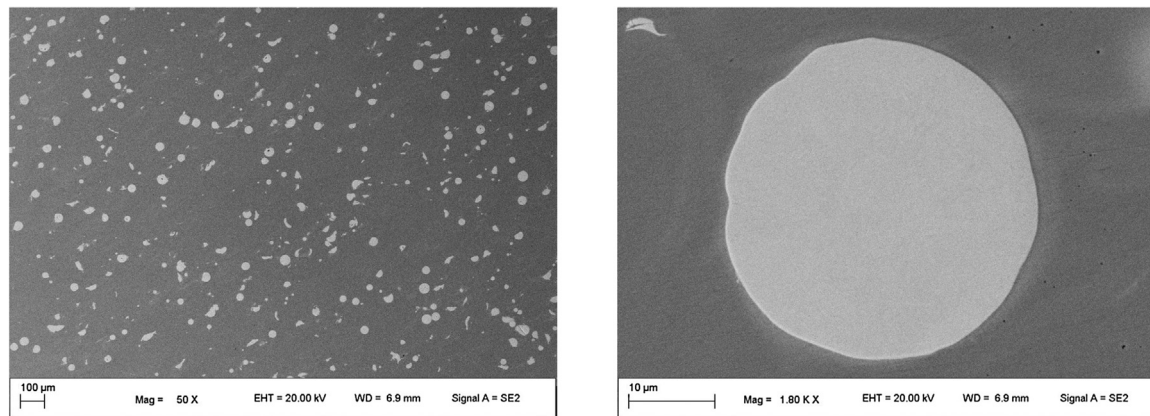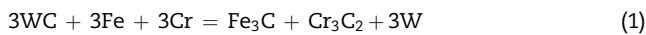

Fig. 8 – Representative SEM micrographs showing the distribution and interface of WC particle in the case of IN718-10WC sample.

place at the interface due to the chemical affinity principle as follows:

$$3WC + 3Fe + 3Cr = Fe_3C + Cr_3C_2 + 3W \tag{1}$$

This in situ intermediate layer was few hundred nm thickness and very strong, which supports the load bearing of composites (Fig. 9).

3.4. Thermal mechanical analysis

As the Inconel material is mainly used for high temperature applications up to 700 °C, some rotating or precise clearance parts need to be dimensionally stable at elevated temperature. The thermal mechanical analysis was thus carried out to measure the coefficient of thermal expansion in the temperature range from 50° to 700 °C and the results were presented in Table 4 [23]. It is observed that for all the samples, the CTE gradually increased with an increase in temperature and mostly followed a linear relationship with increasing temperature. The CTE value for the monolithic IN718 was from 13.7 to 14.97×10^{-6} K^{-1} for the temperature ranges 50–200 °C and

50–700 °C, respectively. These results are in consistent with the results in the literature search [12]. With the addition of WC particles, it is clearly seen that the CTE values reduced remarkably. This is because WC is very stable and has low CTE value (5.5×10^{-6} K^{-1}) within the temperature range and this carbide also bonded well with the Inconel matrix. The results suggest that the developed composites are much more dimensionally stable at elevated temperature than that of the monolithic IN718.

3.5. Mechanical properties

The results of hardness measurements are shown in Table 5. They reveal that the addition of WC reinforcement led to a marginal increment in the macrohardness of the matrix from 299 HBN to 345 HBN in the case of the IN718-10WC samples. Further increment of WC addition to 15 wt.% resulted in a minimal enhancement of the matrix's average macro-hardness. In addition, an attempt was carried out to measure microhardness at three distinguished regions: (i) the inner WC particle, (ii) the interface within few μm away from the WC particle, and (iii) the matrix. It is revealed that the WC was super-hard with the microhardness value of about 2670 HV,
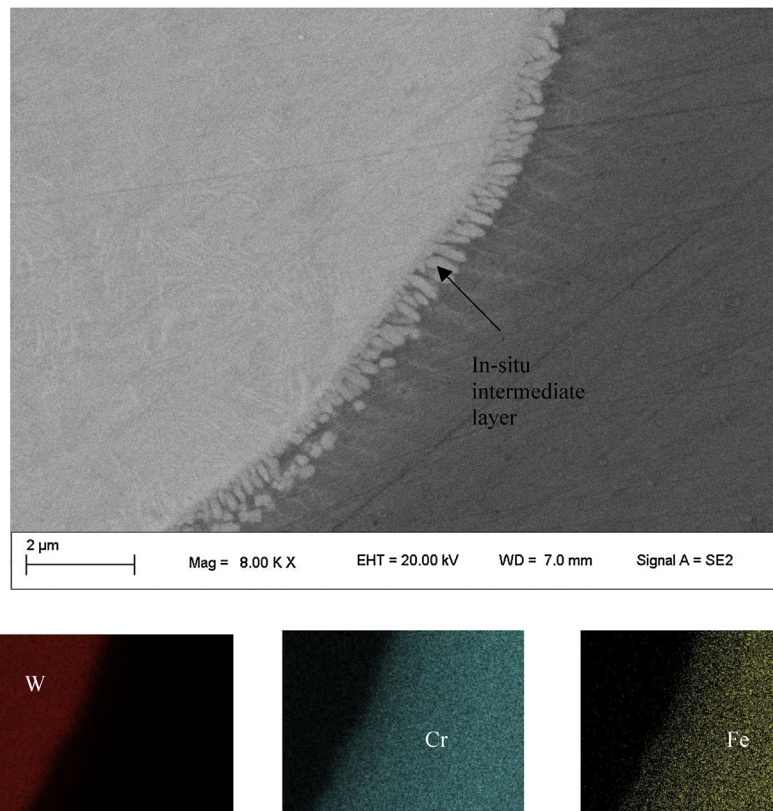
Fig. 9 – SEM image showing the interfacial and in-situ intermediate layer between the WC particle and matrix.

Table 4 – Coefficient of thermal expansion of monolithic and its composites ($\times 10^{-6}$ K^{-1}).

Sample	50–200 °C	50–300 °C	50–400 °C	50–500 °C	50–600 °C	50–700 °C
IN718	13.70 ± 0.09	13.78 ± 0.06	14.16 ± 0.04	14.39 ± 0.12	14.50 ± 0.13	14.97 ± 0.16
IN718-5WC	13.35 ± 0.06	13.41 ± 0.09	13.65 ± 0.07	13.90 ± 0.15	13.65 ± 0.11	13.92 ± 0.14
IN718-10WC	12.78 ± 0.08	12.89 ± 0.07	13.12 ± 0.05	13.45 ± 0.09	13.64 ± 0.13	13.76 ± 0.12
IN718-15WC	11.64 ± 0.11	11.95 ± 0.08	12.15 ± 0.10	12.32 ± 0.08	12.59 ± 0.12	12.85 ± 0.09

Table 5 – Microhardness of monolithic IN718 and its composite samples.

| Sample	Matrix (HBN)	WC particle (HV$_{0.2}$)	Interface (HV$_{0.2}$)	Matrix (HV$_{0.2}$)
IN718	299 ± 5	–	–	315 ± 8
IN718-5WC	322 ± 7	2670 ± 97	1250 ± 76	340 ± 12
IN718-10WC	345 ± 8	2635 ± 105	1198 ± 52	364 ± 14
IN718-15WC	346 ± 15	2665 ± 121	1204 ± 74	366 ± 21

the transient interface exhibited good hardness of about 1250 HV while the matrix showed a medium hardness varying from 315 to 362 HV for monolithic and composite samples, respectively. It is well correlated in the work [12] that the significant increase in hardness leads to overall improvement in wear resistance of composites. The increase in hardness is mainly attributed to two reasons: (i) the presence of well distributed super-hard tungsten carbide particles, and (ii) the good interfacial bonding between the particle and the matrix [11,18,24].

The results of tensile test for monolithic and composite samples are presented in Table 6 and Fig. 10. IN718 tensile data taken from the EOS source showed similar values and it serves as a benchmarking reference. It is seen that Young's modulus of the composites, which measures the resistance ability of a material against external force elastically, was enhanced remarkably with the addition of WC particles. It was increased from 159 GPa in the case of IN718 sample to 225 GPa in the case of IN718-15WC sample and it accounts for 42% improvement. In addition, the 0.2% yield strength and ultimate tensile

Table 6 – Mechanical properties of as-printed monolithic IN718 and its composites.

| Sample (as-printed)	E-Modulus (GPa)	0.2YS (MPa)	UTS (MPa)	Strain at break (%)
IN718	159 ± 12	771 ± 4	1073 ± 1	29.4 ± 0.6
IN718-5WC	215 ± 17	980 ± 16	1195 ± 12	21.6 ± 1.5
IN718-10WC	223 ± 15	1078 ± 14	1287 ± 15	15.1 ± 1.1
IN718-15WC	225 ± 21	974 ± 21	1104 ± 19	7.8 ± 1.1
IN718 (EOS source)	160 ± 20	780 ± 50	1060 ± 50	27 ± 5
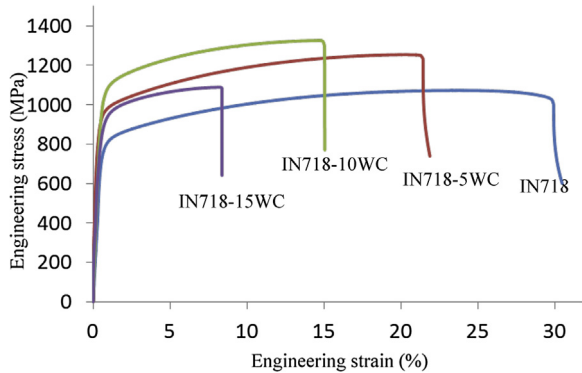
Fig. 10 – Tensile stress–strain curves of monolithic IN718 and its composites.

strength of composite samples were seen to be improved from 771 MPa and 1073 to 1078 MPa and 1287 MPa with the addition of 10 wt.% of WC particles and they are equivalent to 40% and 20% improvement, respectively. The main reasons attributed to the increase of Young's modulus, yield strength and ultimate tensile strength are: (i) presence of well distributed WC particles; (ii) good interfacial bonding between the particle and the matrix; and (iii) grain refinement due to the presence of WC particles acting as obstacles to the heat flow thus promoting less elongated grain structures [11,24]. Moreover, a declining trend was observed for both yield strength and ultimate tensile strength when the amount of reinforcement increased to 15 wt.%. This is because the presence of internal pores in the plasma spheroidized WC powders which served as crack initiation sites. Furthermore, the ductility of composite samples was adversely reduced and this trend was observed in most composite samples with micro-particles additions.

3.6.   Fractography study

Fractography study was carried out to reveal different modes of failure among the monolithic and composite samples and the results are shown in Figs. 11 and 12. The fractured monolithic sample showed severe plastic deformation bands which presents for ductile feature and the presence of pronounced voice induced cracks [25,26]. On the other hand, the composite samples showed limited plastic deformation bands and distinguished shattered WC particle with super strong interfacial bonding. It is observed that most of the cracks were initiated from the voids (trapped gas porosity) in the case of monolithic samples, while most of the cracks appeared inside the WC particles because of internal pores when subjected to high stress concentration (Fig. 11 low and
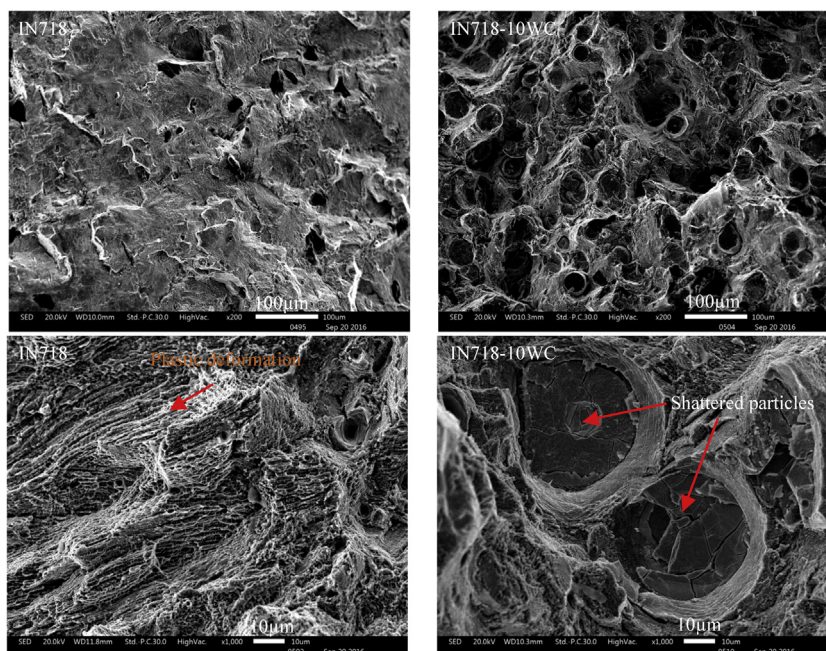
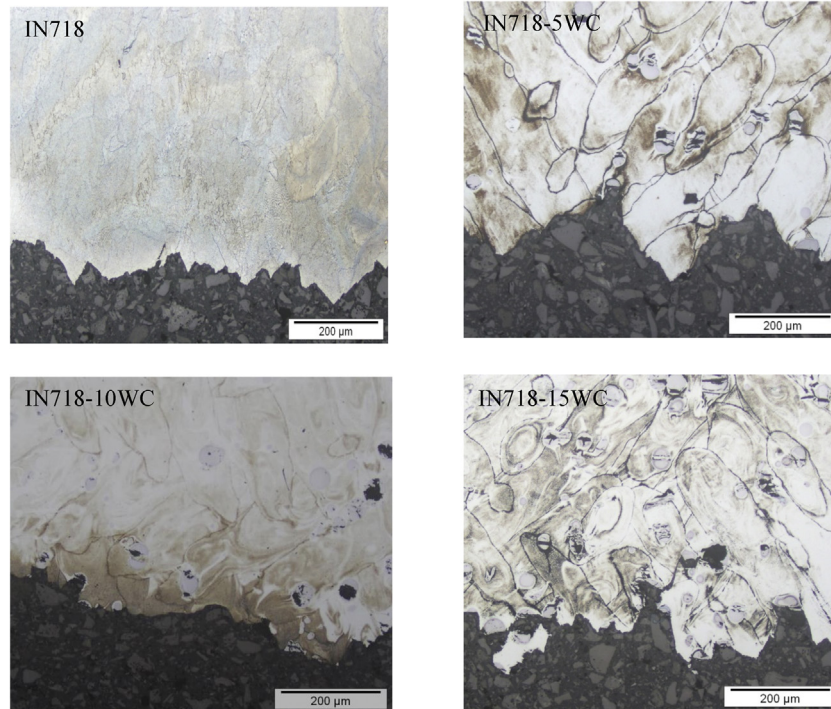**Fig. 11 – Fractographs showing the plastic deformation and particle shattering effects.**

Fig. 12 – Top view fractography showing crack initiation from the inner shattered WC particles.

high magnification) [25]. The fractured tensile samples were resin mounted and the propagation of cracks was examined. Fig. 12 shows that the cracks opened simultaneously at the shattered particles and propagated to the next particles in the case of composite samples while for the monolithic samples, no observable crack initiation and propagation was seen.

4. Conclusion

The followings are conclusions from the present study:

- Dense IN718-WC composites with uniform distribution of WC particles were successfully developed using the selective laser melting technology.
- WC particles acted as obstacles to hinder the growth of elongated grain in X and Y directions.
- Formation of strong intermediate phase at the particle/matrix interface was observed.
- Significant improvements in dimensional thermal stability, hardness and strengths were observed for IN718-WC composite materials while the ductility was compromised.
- From the fractographs, IN718 monolithic samples exhibited plastic deformation and the formation of void induced cracks while the IN718-WC composite counterparts showed the presence of WC particle shattering with good particle/matrix interfacial bonding.

Ethical statement

Authors state that the research was conducted according to ethical standards.

Acknowledgement

REFERENCES

[1] T. Trosch, J. Strößner, R. Völkl, U. Glatzel, Mater. Lett. 164 (2016) 428–431.
[2] J. Kundin, L. Mushongera, H. Emmerich, Acta Mater. 95 (2015) 343–356.
[3] E. Chlebus, K. Gruber, B. Kuźnicka, J. Kurzac, T. Kurzynowski, Mater. Sci. Eng. A 639 (2015) 647–655.
[4] E. Lundström, K. Simonsson, D. Gustafsson, T. Månsson, Eng. Fract. Mech. 118 (2014) 17–30.
[5] M.K. Thompson, G. Moroni, T. Vaneker, G. Fadel, R.I. Campbell, I. Gibson, A. Bernard, J. Schulz, P. Graf, B. Ahuja, F. Martina, CIRP Ann. – Manuf. Technol. 65 (2016) 737–760.
[6] D. Herzog, V. Seyda, E. Wycisk, C. Emmelmann, Acta Mater. 117 (2016) 371–392.
[7] A. Davydova, A. Domashenkov, A. Sova, I. Movtchan, P. Bertrand, B. Desplanques, N. Peillon, S. Saunier, C. Desrayaud, S. Bucher, C. Iacob, J. Mater. Process. Technol. 229 (2016) 361–366.
[8] M. Sadowski, L. Ladani, W. Brindley, J. Romano, Addit. Manuf. 11 (2016) 60–70.
[9] J.C. Fox, S.P. Moylan, B.M. Lane, Procedia CIRP 45 (2016) 131–134.
[10] M. Cloots, P.J. Uggowitzer, K. Wegener, Mater. Des. 89 (2016) 770–784.
[11] D.E. Cooper, N. Blundell, S. Maggs, G.J. Gibbons, J. Mater. Process. Technol. 213 (2013) 2191–2200.

[12] T. Rong, D. Gu, J. Alloys Compd. 680 (2016) 333–342.

[13] P. Hanzl, M. Zetek, T. Bakša, T. Kroupa, Procedia Eng. 100 (2015) 1405–1413.

[14] L.N. Carter, C. Martin, P.J. Withers, M.M. Attallah, J. Alloys Compd. 615 (2014) 338–347.

[15] J. Strößner, M. Terock, U. Glatzel, Adv. Eng. Mater. 17 (2015) 1099–1105.

[16] Q.B. Nguyen, M.L.S. Nai, Z. Zhu, C.-N. Sun, J. Wei, W. Zhou, Engineering 3 (2017) 1–6.

[17] Q.B. Nguyen, D.N. Luu, S.M.L. Nai, Z. Zhu, Z. Chen, J. Wei, Arch. Civil Mech. Eng. 18 (2018) 948–955.

[18] B. Zhang, G. Bi, S. Nai, C.-n. Sun, J. Wei, Opt. Laser Technol. 80 (2016) 186–195.

[19] Q. Jia, D. Gu, J. Alloys Compd. 585 (2014) 713–721.

[20] G. Ziółkowski, E. Chlebus, P. Szymczyk, J. Kurzac, Arch. Civil Mech. Eng. 14 (2014) 608–614.

[21] K. Kulawik, P.A. Buffat, A. Kruk, A.M. Wusatowska-Sarnek, A. Czyrska-Filemonowicz, Mater. Charact. 100 (2015) 74–80.

[22] J. Cao, F. Liu, X. Lin, C. Huang, J. Chen, W. Huang, Opt. Laser Technol. 45 (2013) 228–235.

[23] Q. Shi, D. Gu, M. Xia, S. Cao, T. Rong, Opt. Laser Technol. 84 (2016) 9–22.

[24] G. Bi, C.N. Sun, M.L. Nai, J. Wei, Phys. Procedia 41 (2013) 828–834.

[25] D. Zhang, W. Niu, X. Cao, Z. Liu, Mater. Sci. Eng. A 644 (2015) 32–40.

[26] C. Hong, D. Gu, D. Dai, M. Alkhayat, W. Urban, P. Yuan, S. Cao, A. Gasser, A. Weisheit, I. Kelbassa, M. Zhong, R. Poprawe, Mater. Sci. Eng. A 635 (2015) 118–128.